RESEARCH ARTICLE

Complex B_1^+ mapping with Carr-Purcell spin echoes and its application to electrical properties tomography

Santhosh Iyyakkunnel[1,2] ⦿ | **Matthias Weigel**[1,2,3,4] ⦿ | **Carl Ganter**[5] ⦿ | **Oliver Bieri**[1,2]

[1]Division of Radiological Physics, Department of Radiology, University Hospital Basel, Basel, Switzerland

[2]Department of Biomedical Engineering, University of Basel, Basel, Switzerland

[3]Translational Imaging in Neurology (ThINk) Basel, Department of Biomedical Engineering, Faculty of Medicine, University Hospital Basel and University of Basel, Basel, Switzerland

[4]Neurologic Clinic and Policlinic, MS Center and Research Center for Clinical Neuroimmunology and Neuroscience Basel (RC2NB), University Hospital Basel and University of Basel, Basel, Switzerland

[5]Department of Radiology, Klinikum rechts der Isar, Technical University of Munich, Munich, Germany

Correspondence
Santhosh Iyyakkunnel, Division of Radiological Physics, Department of Radiology, University Hospital of Basel, Petersgraben 4, 4031 Basel, Switzerland.
Email: santhosh.iyyakkunnel@unibas.ch

Funding information
Swiss National Science Foundation; Grant/Award No. 325230_182008.

Purpose: To present a new complex-valued B_1^+ mapping method for electrical properties tomography using Carr-Purcell spin echoes.

Methods: A Carr-Purcell (CP) echo train generates pronounced flip-angle dependent oscillations that can be used to estimate the magnitude of B_1^+. To this end, a dictionary is used that takes into account the slice profile as well as T_2 relaxation along the echo train. For validation, the retrieved B_1^+ map is compared with the actual flip angle imaging (AFI) method in a phantom (79 ε_0, 0.34 S/m). Moreover, the phase of the first echo reflects the transceive phase. Overall, the CP echo train yields an estimate of the complex-valued B_1^+, allowing electrical properties tomography with both permittivity and conductivity. The presented method is evaluated in phantom scans as well as for in vivo brain at 3 T.

Results: In the phantom, the obtained magnitude B_1^+ maps retrieved from the CP echo train and the AFI method show excellent agreement, and both the reconstructed estimated permittivity (79 $\pm$ 3) ε_0 and conductivity (0.35 $\pm$ 0.04) S/m values are in accordance with expectations. In the brain, the obtained electrical properties are also close to expectations. In addition to the retrieved complex B_1^+ information, the decay of the CP echo trains also yields an estimate for T_2.

Conclusion: The CP sequence can be used to simultaneously provide both B_1^+ magnitude and phase estimations, and therefore allows for full reconstruction of the electrical properties.

KEYWORDS

B_1 mapping, CP, CPMG, electrical properties tomography, spin echoes

1 | INTRODUCTION

During an MRI scan, the electromagnetic fields, such as the RF fields used for excitation, are affected by the tissues' electrical properties (EPs), which in turn are sensitive to pathological changes and therefore show potential in diagnosis and treatment of cancer patients.[1,2] Getting the EPs from a conventional MRI scan was first mentioned by Haacke et al.[3] in 1991, but this idea was not widely pursued because of "spurious phase effects" until after the turn of the century, when this technique would be first known as electric properties tomography (EPT).[4–6]

EPT exploits the relation between the EPs and the electromagnetic fields derived from the Maxwell equations. In fact, EPs depend on the curvature (second-order derivative) of the complex RF transmit field (B_1^+) inside

the scanned object, and thus require acquisitions with high SNR. Even though methods to estimate the complex-valued B_1^+ have been reported,[7-9] generally two separate scans are required: one to determine its amplitude and another to determine its phase. For the latter, a spin-echo sequence is often used, as it combines high signal with robustness against field inhomogeneities. To measure the B_1^+ amplitude, one generally reverts to existing B_1 mapping methods.[9-11] These methods are based primarily on gradient-echo sequences, as most applications for B_1 mapping value speed over resolution. In the context of this work, a method termed B_1-TRAP (B_1 mapping with the transient phase of unbalanced SSFP)[12] stands out. This method retrieves the local B_1 field from the oscillations of the transient phase of a coherent steady state sequence. It can thus be expected that a train of spin echoes should exhibit similar signal oscillations as a function of the flip angle. In fact, this flip angle–dependent oscillatory behavior for multi-spin-echo sequences, such as the ones suggested by Carr and Purcell (CP)[13] or Meiboom and Gill (CPMG),[14] has already been demonstrated.[15-17]

In this work, we will show that the local B_1^+ magnitude can be retrieved from a CP echo train in conjunction with an estimate for the transceive phase. As a result, a CP sequence offers a unique setting for EPT. Moreover, the enveloping decay of the CP echoes offers an estimate for the transverse relaxation time T_2.

2 | METHODS

A multi-spin-echo sequence with equidistant echo spacing is shown in Figure 1A, where α denotes the flip angle of the refocusing pulse; Φ stands for the RF phase; and TE denotes the echo time (also indicating the temporal spacing between the application of RF pulses). In the CP scheme, all excitations are applied along the same axis; thus, $\Phi_0 = \Phi_1$ applies.[13] In the CPMG scheme, excitation and refocusing pulses are perpendicular to each other, and $|\Phi_0 - \Phi_1| = 90°$ applies.[14] For the experiments described in the following, a prototype of such a multi-spin-echo sequence was used. By changing the RF phase of the excitation, the sequence was run in either CP or CPMG mode.

2.1 | B_1^+ mapping with multi-spin-echo sequences

The echo amplitudes for both the CP and CPMG sequence as a function of the flip angle has been studied in the past.[15-19] Zur[20] derived analytic integral expressions for the n th echo intensity of CP, as well as CPMG, signals

in the absence of relaxation from a vector model for the sequence's pseudo steady state:

$$I_{CPMG}(n) = M_0 \left(\sin\frac{\alpha}{2} + \frac{1}{\pi} \int_0^\pi \frac{\lambda^2}{1+\lambda^2} e^{in\psi} d\phi \right) \quad (1)$$

$$I_{CP}(n) = M_0 \left(\frac{1}{\pi} \int_0^\pi e^{in\psi} d\phi \right) \quad (2)$$

with

$$\psi = 2\cos^{-1}\left[\cos\frac{\alpha}{2}\cos\phi\right] \quad (3)$$

and

$$\lambda = \frac{\cos\frac{\alpha}{2}\sin\phi}{\sin\frac{\alpha}{2}}, \quad (4)$$

where 2ϕ is the phase accumulation of an isochromat during one TR, and M_0 is the equilibrium magnetization.

Despite the compact forms of Equations 1 and 2, it is not obvious how the B_1^+ amplitude can be retrieved from the echo amplitudes of CP and CPMG echo trains. Using a generating functions formalism, Lukzen et al[16,17] showed that the asymptotic behavior ($n \to \infty$) of Equations 1 and 2 is of the following form:

$$I_{CPMG}(n \to \infty) = M_0 \left(\sin\frac{\alpha}{2} - \frac{1}{2} \frac{1}{\sqrt{\pi\tan\left(\frac{\alpha}{2}\right)}} \frac{\cos\left(n\alpha - \frac{\pi}{4}\right)}{\sqrt{n^3}} \right) \quad (5)$$

$$I_{CP}(n \to \infty) = M_0 \left(\tan\left(\frac{\alpha}{2}\right) \frac{1}{\sqrt{\pi\tan\left(\frac{\alpha}{2}\right)}} \frac{\cos\left(n\alpha + \frac{\pi}{4}\right)}{\sqrt{n}} \right) \quad (6)$$

Notably, these expressions converge to Zur's[20] exact solutions (Equations 1 and 2) already for $n \gtrsim 8$. Equations 5 and 6 now clearly show that the echo amplitudes oscillate with a frequency of $\alpha/2\pi$. This is illustrated in Figure 1B, where the echo intensities are plotted for both CP and CPMG, using Equations 1, 2, 5, and 6 and for flip angles $\alpha = 45°$ (Figure 1B, left) and $\alpha = 90°$ (Figure 1B, right). Figure 1B further confirms that the integral and explicit expressions for the echo amplitudes are identical for larger n. From this, a voxel-wise analysis of the oscillatory behavior of the multi-spin-echo train can be used to yield an estimate for the local flip angle, which in turn can be used as a direct measure for the relative B_1^+ amplitude.[21,22] For convenience, the B_1^+ amplitude as a relative quantity will be referred to as just B_1 in the following.

Even though CPMG and CP signals oscillate with the same flip angle–dependent frequency, they differ in other aspects, such as amplitude, asymptotic limit, and
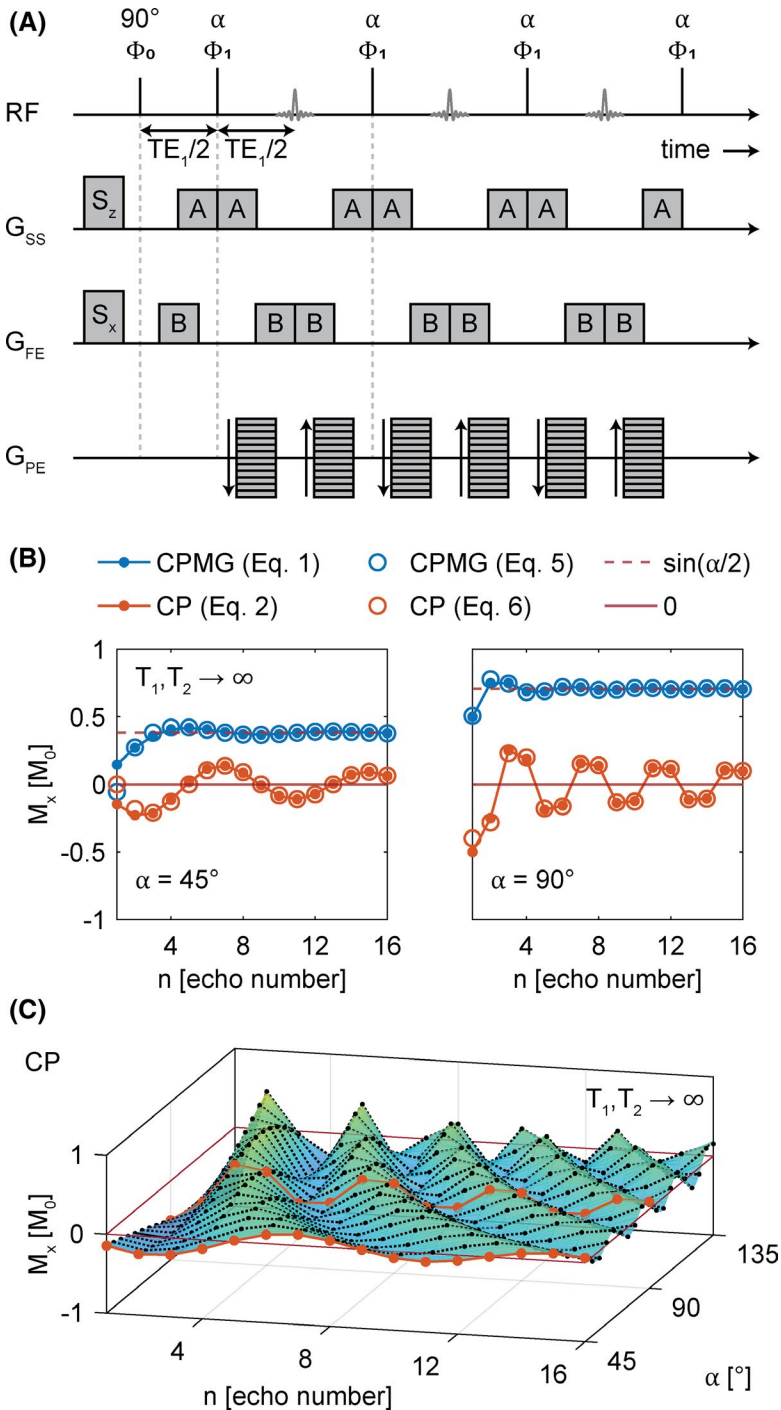
FIGURE 1 A, General simplified schematic of the multi-spin-echo sequence with equidistant echoes. B, Comparison between simulated values of echo amplitudes using analytic integral expressions from Equations 1 and 2 to compute the echo amplitudes (filled circles) and the analytic expressions from Equations 5 and 6, which are valid for large n (open circles). Both approaches do not consider relaxation effects. Echo amplitudes are shown for flip angles $\alpha = 45°$ (left) and $\alpha = 90°$ (right). C, Surface plot showing the flip-angle dependency of the Carr-Purcell (CP) multi-echo signal. Abbreviation: CPMG, Carr-Purcell-Meiboom-Gill

convergence speed (see Figure 1B). The amplitude of the damped oscillations in the two modes differs by a factor $2\tan(\alpha/2)$. Thus, for $\alpha = 90°$, the oscillatory amplitude is twice as high in CP as compared with CPMG. Conversely, in CPMG, a high signal intensity is maintained even for late echoes due to constructive interference of spin echoes and stimulated echoes and convergence to the asymptotic limit of $M_0\sin(\alpha/2)$.[14,18] In the CP sequence, destructive interference causes the signal to decay to zero, notably even in the absence of relaxation. Interestingly, from Equations 5 and 6, we see that CP signals converge with $1/\sqrt{n}$, whereas

CPMG signals converge with $(1/\sqrt{n})^3$. This results in a slower signal decay in CP than in CPMG (see Figure 1B), offering longer oscillatory traces. In summary, the CP sequence is much better suited for B_1 mapping than CPMG and is thus used in the following.

2.2 | Choice of the refocusing flip angle

The refocusing flip angle will determine the frequency of the measured signal (Equations 5 and 6). Based on our

experience, the observed flip angles deviate approximately by about a factor of 0.5–1.3 from the nominal flip angle at 3 T. Thus, the choice of the nominal refocusing flip angle can be viewed as a trade-off between high signal intensity, resulting RF power deposition (leading to the specific absorption rate) and the sampling of the oscillation frequency across the object. At high refocusing flip angles of $\alpha > 150°$, specific absorption rate limits might be reached at 3 T, but the oscillation frequency also becomes aliased ($B_1 \cdot \alpha > 180°$). Thus, a refocusing flip angle of 90° appears to be a good compromise for the purpose of B_1 mapping and is chosen for the following experiments.

2.3 | Transmit phase estimation

The phase of a spin echo is free from external disturbances such as field inhomogeneities. Consequently, with the first echo, the phase directly at the time of excitation will be restored. This phase corresponds to the so-called transceive phase, as it contains contributions from both the transmit field and the receive field or sensitivity.[23,24] For EPT, ideally the complex B_1^+ (i.e., the local B_1^+ magnitude and the transmit phase) enters the reconstruction. To get an estimate of the transmit phase, the so-called transceive phase assumption is frequently used.[23] The transceive phase assumption states that transmit and receive phases are almost equal under the conditions that the field strength is no greater than 3 T, the scanned object is of approximately cylindrical form, and a quadrature birdcage coil is used for excitation and reception.[23] In the clinical setting, however, typically only multichannel receive coils are available, and proper estimation of the transceive phase depends on the coil combine method used.[25,26]

Because the transceive phase is contained in the measurement, the uncertainty in the transceive map can be estimated by the inverse of the SNR of the spin-echo magnitude image.[27,28] The magnitude SNR was obtained by the ratio of the average signal magnitude within the object and the SD of the real part of the image in the background (air).

2.4 | Simulations and dictionary generation

In this study, a dictionary is used to retrieve the frequency of the oscillating echo intensities. Although the frequency of the acquired signals depends on the local B_1^+ magnitude, the signal decay is governed primarily by the transverse relaxation time[18] and can be used to yield an estimate for T_2.

For the generation of the dictionary, the CP pulse sequence was first simulated to yield the exact timing, shape, and amplitude of all RF and gradient pulses. Then, the tissue-specific signal response was simulated with *MATLAB* (The MathWorks, Natick, MA) using the configuration model toolkit (CoMoTk)[29] for a range of nominal flip angles and T_2 values (taking into account slice profile effects). The slice profile was taken into account by simulating the effect of the RF pulses using the hard pulse approximation.[30,31] T_1 was fixed at 1 second, as simulations showed negligible impact of common brain-tissue T_1 values on the signal. For T_2, 21 logarithmically spaced points between 10 and 1000 ms were cubically interpolated to have a total of 41 points in this range. Then, the range of T_2 was extended by 10 linearly spaced points between 1200 and 3000 ms. The relative B_1 was varied linearly between 0.5 and 1.3 with steps of 0.01. Finally, the simulated CP signals were multiplied with $\sqrt{n}$ to compensate for the inherent CP decay (see Equation 6). Finding the best match of the measurement in the dictionary was performed by searching for the maximum Pearson correlation coefficient. To this end, the normalized measured complex-valued signal was multiplied with all the normalized simulated signals from the dictionary. Normalization was performed by subtracting the signal's mean and dividing by its SD. Because the input was partly complex-valued, the resulting Pearson correlation coefficients were also complex-valued, and the maximum was determined based on its magnitude.

Simulations and calculations were performed in *MATLAB* (R2019a) unless stated otherwise.

2.5 | Imaging experiments

Imaging was performed in a phantom and for in vivo brain at 3 T (Magnetom Prisma; Siemens Healthcare, Erlangen, Germany) using the body coil for transmission and the manufacturer's 20-channel head and neck coil for reception. Phase images from multichannel coil data were reconstructed using the manufacturer's "adaptive coil combine" method. To evaluate the appropriateness of the multichannel coil combination method for EPT, phantom scans were also performed with a 1H/23Na transmit/receive birdcage coil (RAPID Biomedical, Rimpar, Germany). If not otherwise explicitly stated, scanning was performed with the multichannel head and neck coil. In vivo human MR scans were approved by the local ethics committee, and informed written consent was obtained before the human experiments.

For all experiments, a 2D CP multi-spin-echo prototype sequence was used with spoiler and crusher gradient moments along the slice selection direction ($S_z = 43.98$ mT/m·ms and A = 24.75 mT/m·ms), as well as along the frequency encoding direction ($S_x = 17.89$ mT/m·ms and B = 46.17 mT/m·ms) (see Figure 1A). Within a TR of 2800 ms, 10 echoes were acquired with an echo spacing

of 11 ms, starting at $TE_1 = 11$ ms. To accelerate the scan the partially parallel acquisition technique, GRAPPA[32] was used. To minimize crosstalk between excited slices, a total of 36 slices with 3-mm slice thickness were split in two subsequently measured interleaved slice groups with a 3-mm gap between slices. In plane, cartesian k-space sampling was used for a 144×120 matrix and a 1.5×1.5 mm² resolution. For EP reconstruction, the slices were interpolated to obtain an isotropic voxel size of $1.5 \times 1.5 \times 1.5$ mm³. For excitation, a sinc-shaped RF pulse with a time-bandwidth product of 2 and thickness factor of 0.8 was used, while the refocusing pulses were sinc-shaped pulses with a time-bandwidth product of 4 and a thickness factor of 1.6. Both the excitation and refocusing pulses had a duration of 2.8 ms, and a Hanning filter was used to mitigate pulse truncation effects. The receiver bandwidth was set to 205 Hz/px, and acquisition was completed in less than 7 minutes.

For the phantom scans, a water bottle with a salt concentration of 2 g/L was used. The saline phantom had an estimated conductivity of 0.34 S/m and a permittivity of 79 ε_0 at room temperature.[33,34] Tissue-comparable relaxation times of approximately $T_1 \sim 870$ ms and $T_2 \sim 70$ ms were achieved by adding 0.125 mM MnCl.

For validation purposes, the phantom's B_1 map was also determined with the actual flip-angle (AFI) method.[12] For AFI, the same imaging matrix was acquired as for the multi-spin-echo sequence. Furthermore, a nonselective excitation pulse with a flip angle of 45° was used with $TR2/TR1 = 175$ ms/35 ms, TE = 4.91 ms, a receiver bandwidth of 120 Hz/px, and RF phase-difference increment of 129.3°.[35] The AFI method took about 15 minutes to complete. The local flip angle α was estimated from the signal ratio $r = S2/S1$ and the TR ratio $n = TR2/TR1 = 5$ using $\alpha \approx arccos\left[(rn - 1)/(n - r)\right]$.

Skull stripping for the figures was performed using the standard software package FSL (FMRIB Software Library v6.0, Oxford, United Kingdom).

2.6 | Electrical properties reconstruction

Calculation of the relative permittivity ε_r and the conductivity σ was based on the homogeneous Helmholtz equation,[24,36] yielding:

$$\varepsilon_r = -\frac{1}{\varepsilon_0 \mu_0 \omega^2} Re\left\{\frac{\nabla^2 B_1^+}{B_1^+}\right\} = \frac{1}{\varepsilon_0 \mu_0 \omega^2}\left(-\frac{\nabla^2 |B_1^+|}{|B_1^+|} + |\nabla \varphi^+|^2\right)$$

(7)

$$\sigma = \frac{1}{\mu_0 \omega} Im\left\{\frac{\nabla^2 B_1^+}{B_1^+}\right\} = \frac{1}{\mu_0 \omega}\left(\nabla^2 \varphi^+ + 2\frac{\nabla |B_1^+| \cdot \nabla \varphi^+}{|B_1^+|}\right).$$

(8)

In Equations 7 and 8, ε_0 is the vacuum permittivity; μ_0 is the magnetic vacuum permeability; and ω is the Larmor frequency. The leading (first) terms in these expressions relate the permittivity and the conductivity to the curvature of the B_1^+ magnitude and its phase, respectively. The second terms can be seen as a correction, which is on the order of 10%–20% for typical EPs of human tissues at field strengths up to 3 T.[5,36] For the proposed CP method, $|B_1^+|$ is retrieved from the signal's oscillatory behavior (e.g., signal matching with the dictionary), and φ^+ is estimated directly from the phase image of the first echo, using the transceive phase assumption.[23] For AFI, the transceive phase from the CP sequence was taken for permittivity reconstruction.

The Laplacian and gradients were estimated using the coefficients of a locally fitted second-order polynomial, restricted to voxels with magnitude values similar to the center point of the window (within 15%).[37] This is a strategy to mitigate tissue-boundary errors inherent to taking derivatives and assumes one EP value per tissue. The Laplace estimate was subsequently smoothed with a tissue boundary–preserving median filter.[25,37] For the phantom, the window size for the Laplace estimation was set to $7 \times 7 \times 7$ voxels and to $21 \times 21 \times 21$ voxels for subsequent median filtering. For the brain, the window size was $7 \times 7 \times 13$ voxels for estimating the Laplacian and $15 \times 15 \times 21$ voxels for the tissue-preserving median filter. The magnitude image used for the EP reconstruction was a constructed T_2-weighted image that was generated based on the received T_2 map and the magnitude image of the first echo in the measurement.

3 | RESULTS

The CP echo signals only oscillates with an exact frequency of $\alpha/2\pi$ (see Equation 5) for ideal rectangular slice profiles. In practice, the slice profile is generally not rectangular, and the signal sums over a distribution of flip angles centered around the chosen flip angle α. As a result, the observed frequencies deviate from the ideal $\alpha/2\pi$ behavior (see Figure 2).

Figure 3A shows a voxel-wise comparison of the observed B_1^+ magnitude for both AFI and CP, and over the whole phantom in the form of a binned scatter plot. Using a linear regression analysis, a slope of 0.993 and an offset of −0.013 are found, indicating excellent correlation. In Figure 3B, the relative difference of the two methods is assessed in a Bland-Altmann plot,[38] where the relative difference is defined as $(B_{1,AFI} - B_{1,CP})/(\text{mean } B_1)$ for every voxel. The "mean B_1" corresponds to the voxel-wise average of the $B_{1,AFI}$ and the $B_{1,CP}$. The mean relative difference is calculated to be at −2.14% and is indicated in the figure together with the 95% confidence interval.
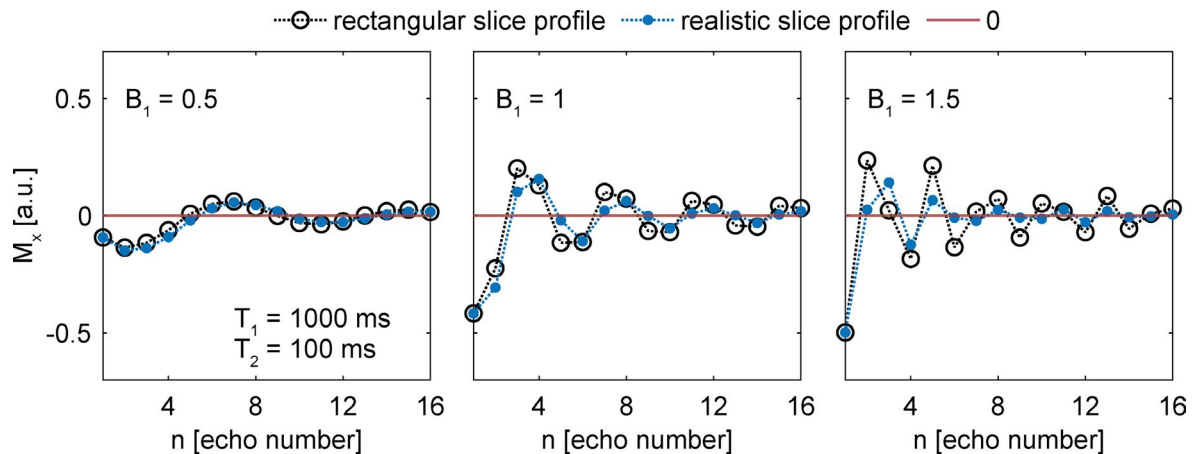
FIGURE 2 Simulations of CP echo amplitudes for an ideal slice profile (black open circles) and for a realistic slice profile (blue filled circles) for relative B_1 values of 0.5, 1, and 1.5. The real slice profile was computed using the pulse shape generated from the sequence. The simulations were performed using the configuration model toolkit[29]
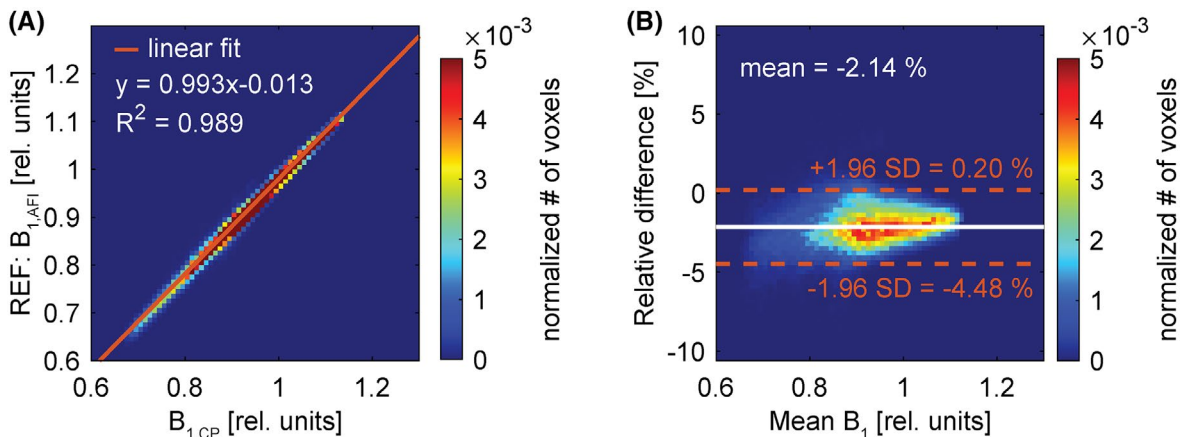

FIGURE 3 A, Binned scatter plot illustrating the correlation between the $B_{1,CP}$ (x-axis) and the $B_{1,AFI}$ (y-axis). The solid line is the result of a linear least-square analysis. B, Corresponding Bland-Altman plot of the relative difference of the two methods as a function of the voxel-wise mean B_1. The solid line corresponds to the mean relative difference in percentage. The dashed lines indicate the 95% confidence interval

Example B_1 maps, shown in coronal and transversal orientation, are shown for the AFI scan in Figure 4A and for the CP scan in Figure 4B. The transceive phase images, retrieved from the CP scan, are shown in Figure 4C. The uncertainty of the transceive phase measurement was estimated to be about 0.005 rad. The corresponding permittivities based on the two B_1 maps are shown in Figure 4D,E, respectively, and the CP-based conductivity is shown in Figure 4F. For a large region in the center of the shown axial slice, a mean permittivity value of (80 ± 3) ε_0 is found for AFI, whereas for the CP approach a mean permittivity value of (79 ± 3) ε_0 and a mean conductivity value of (0.35 ± 0.04) S/m is observed. A comparison of the results using either the birdcage coil or the multichannel receive coil is shown in Supporting Information Figure S1. Overall, only marginal differences are observed between the phase information as retrieved by the manufacturer's

"adaptive combine" method and the phase information obtained using the birdcage coil.

After validation in the phantom (Figure 4), the presented method was applied to in vivo brain scans. Figure 5 shows four exemplary axial slices of the brain of a volunteer and compiles the attainable maps. Figure 5A shows the anatomical magnitude images from the first echo for four exemplary axial slices. The contrast of the magnitude image depends considerably on the sequence parameters. The SNR was estimated to be about 80 for the brain scan. In Figure 5B, the B_1 maps based on the presented method are shown. In the field maps, a distinct asymmetry between the left and right brain hemispheres is visually notable. Figure 5C compiles the (transceive) phase images obtained with the first echo of the same slices. The uncertainty of the phase measurement in the brain was found to be 0.013 rad. Finally, Figure 5D shows
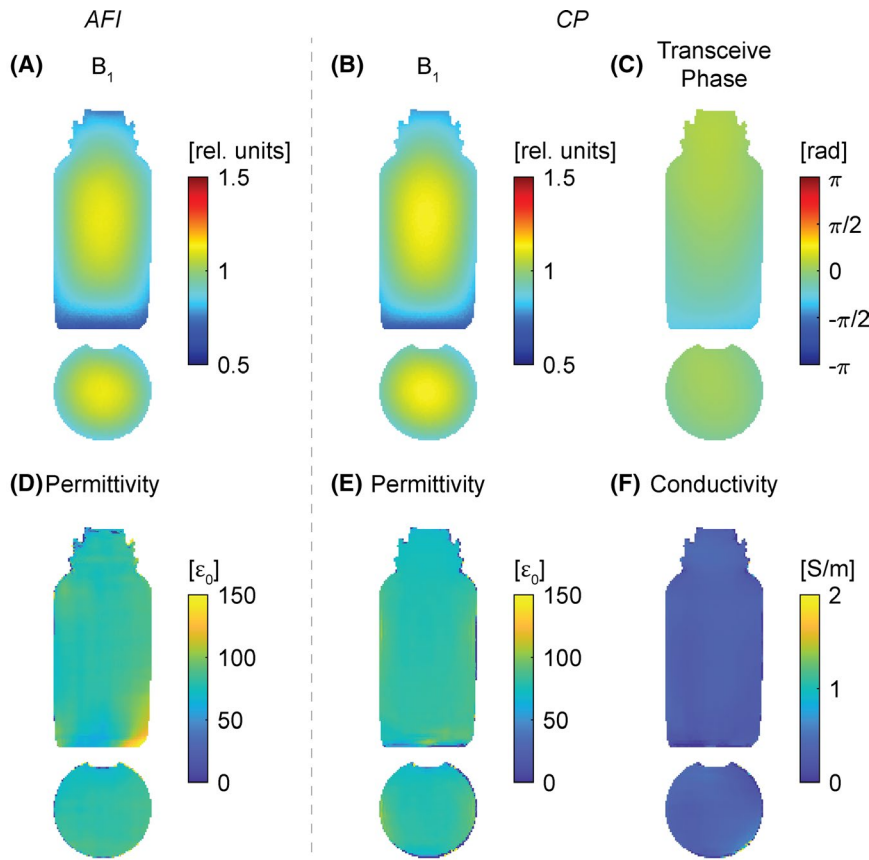
FIGURE 4 Exemplary coronal and axial slices of the saline phantom. A, B_1 map obtained with actual flip-angle imaging (AFI). B, B_1 map obtained with the CP spin-echoes method. C, Transceive phase obtained from the first echo acquisition. D, Reconstructed permittivity from the B_1 map in (A). E, Reconstructed permittivity from the B_1 map in (B). F, Reconstructed conductivity from the phase in (C)

the quantitative T_2 maps for the corresponding slices. The T_2 maps are a direct result of the dictionary-based reconstruction.

For the same exemplary slices as in Figure 5, the results of the EP reconstruction are shown in Figure 6. Figure 6A shows the generated T_2-weigthed magnitude image on which the EP reconstruction is based. Corresponding maps of the electrical properties, permittivity, and conductivity are shown in Figure 6B,C. The asymmetry in the B_1 map (see Figure 5B) of the brain presents an abrupt change in the field distribution, which can lead to biased estimation of the permittivity. For a selected region of interest (ROI) in white matter (WM), a permittivity of $(50 \pm 2)\, \varepsilon_0$ is found (ROI 1 in Figure 6B), whereas the reconstructed conductivity in the same location yields a value of (0.33 ± 0.01) S/m (ROI 1 in Figure 6C). For gray matter (GM), a permittivity of $(69 \pm 6)\, \varepsilon_0$ (ROI 2 in Figure 6B) and a conductivity of (0.75 ± 0.03) S/m (ROI 2 in Figure 6C) are obtained, whereas in CSF, a permittivity of $(112 \pm 14)\, \varepsilon_0$ (ROI 3 in Figure 6B) and a corresponding conductivity of (1.57 ± 0.04) S/m are found (ROI 3 in Figure 6C).

4 | DISCUSSION

In this work, a novel method for simultaneous B_1^+ magnitude and phase estimation using a multi-spin-echo

approach is presented. In particular, the focus lies on the CP multi-spin-echo sequence. The local flip angle can be retrieved from its oscillatory signal behavior, which is more pronounced in the CP sequence than in CPMG. To this end, we suggest using a dictionary for the analysis of the signal oscillations in conjunction with T_2 quantification. A similar dictionary approach was implemented for improving CPMG-based T_2 quantification.[39] Because the sequence is a spin-echo sequence, the transceive phase is already contained in the measurement, more specifically in the first echo.

The flip angle–dependent frequency of the multi-spin-echo sequence can be analyzed in several ways. Looking for the prominent frequency of the Fourier transform of the time-series appears like the most obvious approach but is not very robust and often inaccurate.[12] The B_1 mapping technique B1-TRAP[12] uses an analysis algorithm called "matrix pencil",[40] an approach that identifies a user-defined number of frequency components with corresponding amplitude and damping. However, signals of 2D acquisitions are affected by pulse-shape effects and may cause a bias in the matrix pencil frequency estimation, as only a limited number of components will be found. In contrast to directly assessing the frequency, signal analysis can also be performed using a dictionary, as suggested in this work. The dictionary can be set up with different MR signal simulation techniques such as using Bloch equations,[39,41]

FIGURE 5 Exemplary axial slices of an in vivo brain. A, Magnitude brain images obtained from the first echo acquisition. B, B_1 maps retrieved from the signal correlation with the dictionary. C, Transceive phase images obtained from the first echo acquisition. D, T_2 maps retrieved from signal correlation with the dictionary
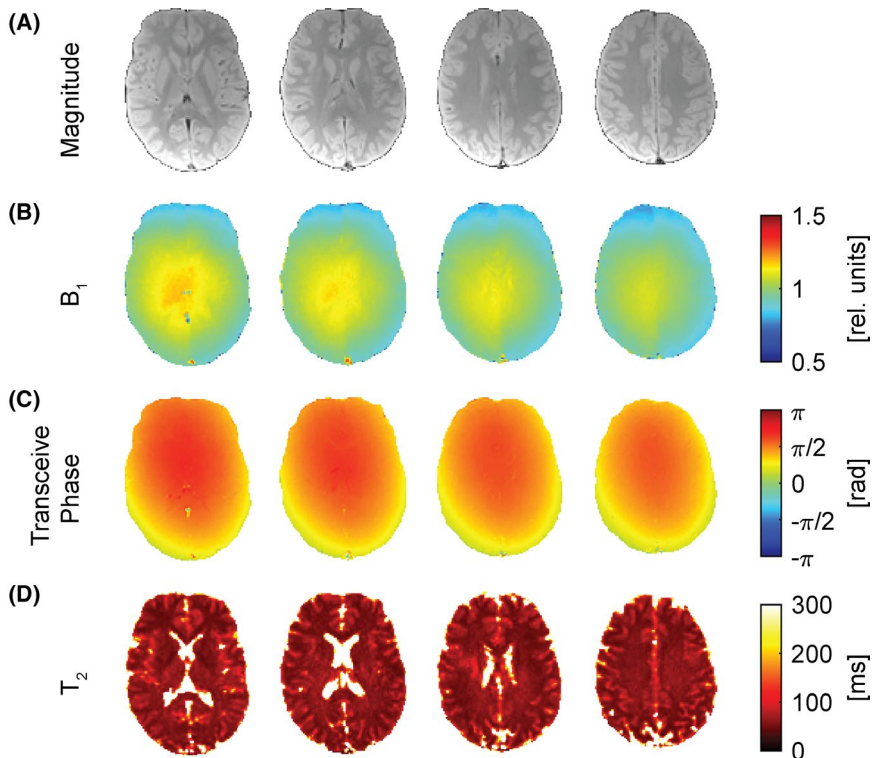
the extended phase graph formalism,[18,19] or as in this work, the configuration model toolkit.[29] The advantage of a dictionary over direct frequency analysis is that relaxation and actual slice-profile effects can be rather easily accounted for. The accuracy of the local flip-angle estimation is then dependent primarily on the resolution of the dictionary. To accurately retrieve B_1 information, the T_2 decay must also be considered. A welcomed byproduct then is local T_2 quantification that is obtained along with the B_1 map. In theory, for refocusing pulse flip angles other than 180°, T_1 relaxation also affects the signal. However, the influence of T_1 is relatively small, and the dictionary is not sensitive enough to recover an accurate T_1 map. In any case, ideally, because of the sensitivity to relaxation, the dictionary should be adjusted whenever the TR or especially TE is changed.

The use of a dictionary with a step size for the B_1 values of 0.01 gives the $B_{1,CP}$ visually a less noisy appearance than the $B_{1,AFI}$, in which the B_1 value can assume values on an almost continuous scale. Nonetheless, the comparison between the presented method and AFI showed good agreement of the two methods. The spin-echo phase is often used as the benchmark transceive phase and thus does not require validation. In this case, as the transceive phase is directly contained in the measurement, its uncertainty is directly linked to the SNR of the acquisition.

Our results indicate that the transceive phase is properly estimated using the manufacturer's "adaptive combine" algorithm for multichannel coil data (see Supporting Information Figure S1). The vendor-specific software is, however, inaccessible for the typical user;

thus, the exact implementation of the coil combination method is unknown. Therefore, generally, a possible bias in the transceive phase from the vendor's coil combine algorithm cannot be ruled out. As the observed permittivity of (79 ± 3) ε_0 and the conductivity of (0.35 ± 0.04) S/m values are in excellent agreement with the expected values $(79 \, \varepsilon_0, 0.34 \, \text{S/m})$,[33] the possible error is assumed to be small.

The obtained B_1 maps of the brain scans indicate good translation of the method to in vivo conditions. As mentioned, the additional effort in generating the dictionary is compensated with the retrieval of additional quantitative T_2 information. Therefore, the presented method is a multi-parametric technique that allows the retrieval of several maps with a single sequence.

For brain tissues at 3 T, the expected permittivity values are 52 ε_0 (WM), 73 ε_0 (GM) and 84 ε_0 (CSF), and the corresponding conductivity is expected to be about 0.34 S/m (WM), 0.59 S/m (GM), and 2.14 S/m (CSF).[42,43] The obtained values for the conductivity $((0.33 \pm 0.01)$ S/m (WM), (0.75 ± 0.03) S/m (GM), and (1.57 ± 0.04) S/m (CSF)) agree with expectations for brain tissues. The deviations might be attributed to large-scale filtering and partial-volume effects due to unproper separation of tissues. Except for CSF, also the found permittivity values $((50 \pm 2)$ ε_0 (WM), $(69 \pm 6 \, \varepsilon_0)$ (GM), and (112 ± 14) ε_0 (CSF)) are close to expectations. Overall, however, the permittivity map shows some inhomogeneity in brain tissues. It has already been reported that permittivity mapping at
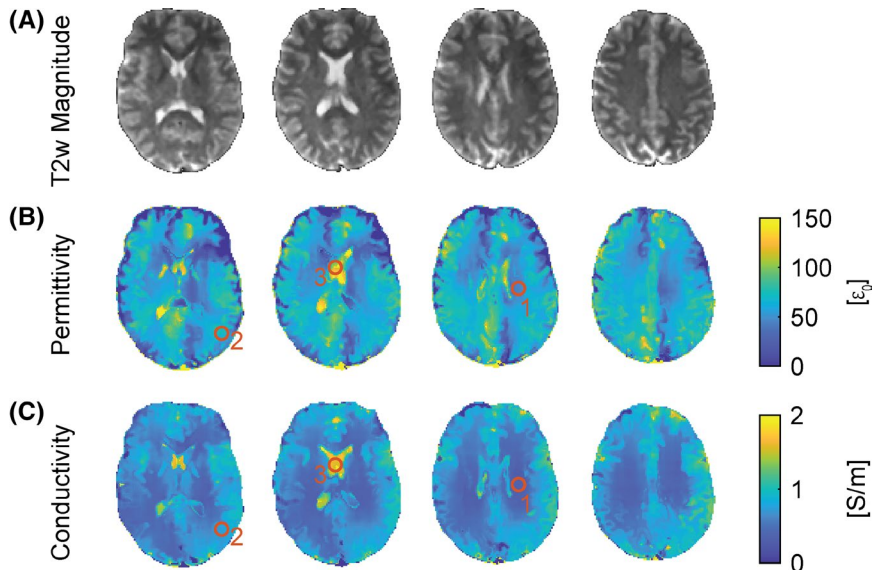
FIGURE 6 Same exemplary in vivo brain axial slices as shown in Figure 5. A, Generated T_2-weighted magnitude images for electrical properties reconstruction. B, Reconstructed permittivity. C, Reconstructed conductivity. The regions of interest (ROIs) indicate where the EP values are taken from with ROI 1 corresponding to white matter (WM), ROI 2 corresponding to gray matter (GM), and ROI 3 corresponding to CSF

3 T based on the Helmholtz equation is rather challenging in clinical acceptable scan times.[44]

Another source of error might arise from the use of a magnitude image to mitigate boundary errors in the reconstruction of the Laplacian.[37] For this geometric constraint, any high-contrast image can be used. The contrast of the first-echo image of the CP scan is dominated by the proton density, whereas the T_2 map from the dictionary mainly separates fluids from tissue. Thus, in this work, we used both the proton density and the quantitative T_2 map to generate a T_2-weighted image that offered the desired level of tissue contrast.

Other factors might also play a role in compromising the accuracy of the electrical properties. Especially the B_1 asymmetry introduces an erroneous region in the permittivity across the brain (see Figure 6). The source of the asymmetry in the excitation across the brain is not exactly known but is seen throughout other works when an unfiltered B_1 map of the brain is shown.[45] The strong variation in the B_1 map can be smoothened out with appropriate postprocessing at the cost of resolution. However, optimizing the reconstruction of the EPs is beyond the scope of this work.

5 | CONCLUSIONS

We showed that conventional CP multi-spin-echo sequences can be exploited for B_1 mapping. In conjunction with the acquired spin-echo phase, all of the means to perform EPT for both permittivity and conductivity are provided. The presented method thus offers a good estimate of the complex-valued B_1^+. As the signal of the echo train is dependent primarily on the local flip angle and

transverse relaxation, the analysis with the dictionary also provides a quantitative T_2 map. EPT was performed with the complex EPT reconstruction technique based on the homogeneous Helmholtz equation and showed good agreement with expectations for the phantom. In vivo, the obtained EPs showed some variation from expectations but generally also agreed well with what has been reported and yielded qualitatively good EP maps. In summary, the use of CP multi-spin-echo approaches might boost efficiency and could render EPT clinically relevant.

ORCID

Santhosh Iyyakkunnel https://orcid.org/0000-0001-9425-2134
Matthias Weigel https://orcid.org/0000-0002-4910-1414
Carl Ganter https://orcid.org/0000-0002-6735-7448

REFERENCES

1. Shin J, Kim MJ, Lee J, et al. Initial study on in vivo conductivity mapping of breast cancer using MRI. *J Magn Reson Imaging*. 2015;42:371-378.
2. Balidemaj E, de Boer P, van Lier ALHMW, et al. In vivo electric conductivity of cervical cancer patients based on B1+ maps at 3T MRI. *Phys Med Biol*. 2016;61:1596-1607.
3. Haacke EM, Petropoulos LS, Nilges EW, Wu DH. Extraction of conductivity and permittivity using magnetic resonance imaging. *Phys Med Biol*. 1991;36:723-734.
4. Wen H. Noninvasive quantitative mapping of conductivity and dielectric distributions using RF wave propagation effects in high-field MRI. In: *Medical Imaging 2003: Physics of Medical Imaging*. Vol. 5030. International Society for Optics and Photonics; 2003:471-477.
5. Voigt T, Katscher U, Doessel O. Quantitative conductivity and permittivity imaging of the human brain using electric properties tomography. *Magn Reson Med*. 2011;66:456-466.

6. Katscher U, Voigt T, Findeklee C, Vernickel P, Nehrke K, Dössel O. Determination of electric conductivity and local SAR Via B1 mapping. *IEEE Trans Med Imaging*. 2009;28:1365-1374.

7. Zhang X, de Moortele P-FV, Schmitter S, He B. Complex B1 mapping and electrical properties imaging of the human brain using a 16-channel transceiver coil at 7T. *Magn Reson Med*. 2013;69:1285-1296.

8. Choi N, Lee J, Kim M-O, Shin J, Kim D-H. A modified multi-echo AFI for simultaneous B1+ magnitude and phase mapping. *Magn Reson Imaging*. 2014;32:314-320.

9. Nehrke K, Börnert P. DREAM—a novel approach for robust, ultrafast, multislice B1 mapping. *Magn Reson Med*. 2012;68:1517-1526.

10. Yarnykh VL. Actual flip-angle imaging in the pulsed steady state: a method for rapid three-dimensional mapping of the transmitted radiofrequency field. *Magn Reson Med*. 2007;57:192-200.

11. Sacolick LI, Wiesinger F, Hancu I, Vogel MW. B1 mapping by Bloch-Siegert shift. *Magn Reson Med*. 2010;63:1315-1322.

12. Ganter C, Settles M, Dregely I, Santini F, Scheffler K, Bieri O. B1-mapping with the transient phase of unbalanced steady-state free precession. *Magn Reson Med*. 2013;70:1515-1523.

13. Carr HY, Purcell EM. Effects of diffusion on free precession in nuclear magnetic resonance experiments. *Phys Rev*. 1954;94:630-638.

14. Meiboom S, Gill D. Modified spin-echo method for measuring nuclear relaxation times. *Rev Sci Instrum*. 1958;29:688-691.

15. Lukzen NN, Savelov AA. Analytical derivation of multiple spin echo amplitudes with arbitrary refocusing angle. *J Magn Reson*. 2007;185:71-76.

16. Lukzen NN, Petrova MV, Koptyug IV, Savelov AA, Sagdeev RZ. The generating functions formalism for the analysis of spin response to the periodic trains of RF pulses. Echo sequences with arbitrary refocusing angles and resonance offsets. *J Magn Reson*. 2009;196:164-169.

17. Petrova MV, Doktorov AB, Lukzen NN. CPMG echo amplitudes with arbitrary refocusing angle: explicit expressions, asymptotic behavior, approximations. *J Magn Reson*. 2011;212:330-343.

18. Hennig J. Echoes—how to generate, recognize, use or avoid them in MR-imaging sequences. Part I: Fundamental and not so fundamental properties of spin echoes. *Concepts Magn Reson*. 1991;3:125-143.

19. Weigel M. Extended phase graphs: dephasing, RF pulses, and echoes—pure and simple. *J Magn Reson Imaging JMRI*. 2015;41:266-295.

20. Zur Y. Analysis of the multi-echo spin-echo pulse sequence. *Concepts Magn Reson Part A*. 2017;46A:e21402.

21. Hartwig V, Vanello N, Giovannetti G, et al. B1+/actual flip angle and reception sensitivity mapping methods: simulation and comparison. *Magn Reson Imaging*. 2011;29:717-722.

22. Hornak JP, Szumowski J, Bryant RG. Magnetic field mapping. *Magn Reson Med*. 1988;6:158-163.

23. van Lier ALHMW, Raaijmakers A, Voigt T, et al. Electrical properties tomography in the human brain at 1.5, 3, and 7T: a comparison study. *Magn Reson Med*. 2014;71:354-363.

24. Katscher U, Kim D-H, Seo JK. Recent progress and future challenges in MR electric properties tomography. *Comput Math Methods Med*. 2013;2013:1-11.

25. Lee J, Shin J, Kim D-H. MR-based conductivity imaging using multiple receiver coils. *Magn Reson Med*. 2016;76:530-539.

26. Voigt T, Homann H, Katscher U, Doessel O. Patient-individual local SAR determination: in vivo measurements and numerical validation. *Magn Reson Med*. 2012;68:1117-1126.

27. Gudbjartsson H, Patz S. The Rician distribution of noisy MRI data. *Magn Reson Med*. 1995;34:910-914.

28. Conturo TE, Smith GD. Signal-to-noise in phase angle reconstruction: dynamic range extension using phase reference offsets. *Magn Reson Med*. 1990;15:420-437.

29. Ganter C. Configuration model. In: Proceedings of the 22nd Annual Meeting of ISMRM, Paris, France, 2018. Abstract 5663.

30. Subramanian V, Eleff S, Rehn S, Leigh J. An exact synthesis procedure for frequency selective pulses. In: Proceedings of the 4th Annual Meeting of SMRM, Boston, Massachusetts, 1985. pp 1452-1453.

31. Pauly J, Le Roux P, Nishimura D, Macovski A. Parameter relations for the Shinnar-Le Roux selective excitation pulse design algorithm (NMR imaging). *IEEE Trans Med Imaging*. 1991;10:53-65.

32. Griswold MA, Jakob PM, Heidemann RM, et al. Generalized autocalibrating partially parallel acquisitions (GRAPPA). *Magn Reson Med*. 2002;47:1202-1210.

33. Stogryn A. Equations for calculating the dielectric constant of saline water (correspondence). *IEEE Trans Microw Theory Tech*. 1971;19:733-736.

34. Gadani D, Rana V, Bhatnagar S, Prajapati A, Vyas AD. Effect of salinity on the dielectric properties of water. *Indian J Pure Appl Phys*. 2012;50:405-410.

35. Nehrke K. On the steady-state properties of actual flip angle imaging (AFI). *Magn Reson Med*. 2009;61:84-92.

36. Katscher U, van den Berg CAT. Electric properties tomography: biochemical, physical and technical background, evaluation and clinical applications. *NMR Biomed*. 2017;30:e3729.

37. Katscher U, Djamshidi K, Voigt T, et al. Estimation of breast tumor conductivity using parabolic phase fitting. In: Proceedings of the 20th Annual Meeting of ISMRM, Melbourne, Australia, 2012. Abstract 3482.

38. Martin Bland J, Altman DG. Statistical methods for assessing agreement between two methods of clinical measurement. *Lancet*. 1986;327:307-310.

39. Ben-Eliezer N, Sodickson DK, Block KT. Rapid and accurate T2 mapping from multi–spin-echo data using Bloch-simulation-based reconstruction. *Magn Reson Med*. 2015;73:809-817.

40. Lin Y-Y, Hodgkinson P, Ernst M, Pines A. A novel detection-estimation scheme for noisy NMR signals: applications to delayed acquisition data. *J Magn Reson*. 1997;128:30-41.

41. Bloch F. Nuclear induction. *Phys Rev*. 1946;70:460-474.

42. Gabriel S, Lau RW, Gabriel C. The dielectric properties of biological tissues. II: Measurements in the frequency range 10 Hz to 20 GHz. *Phys Med Biol*. 1996;41:2251-2269.

43. Gabriel S, Lau RW, Gabriel C. The dielectric properties of biological tissues. III: Parametric models for the dielectric spectrum of tissues. *Phys Med Biol*. 1996;41:2271-2293.

44. Gavazzi S, Berg CAT, Sbrizzi A, et al. Accuracy and precision of electrical permittivity mapping at 3T: the impact of three mapping techniques. *Magn Reson Med*. 2019;81:3628-3642.

45. Boudreau M, Tardif CL, Stikov N, Sled JG, Lee W, Pike GB. B1 mapping for bias-correction in quantitative T1 imaging of the brain at 3T using standard pulse sequences. *J Magn Reson Imaging*. 2017;46:1673-1682.

SUPPORTING INFORMATION

Additional supporting information may be found in the online version of the article at the publisher's website.

FIGURE S1 Example coronal and axial slices of the saline water phantom using the proposed CP sequence. A, Transceive phase measured with a birdcage coil. B, Transceive phase using the manufacturers "adaptive combine" method for the data from the 20-channel head and neck coil. A global offset was added to the head and neck coil phase measurement for comparison purposes. The measurements were carried out as described in the methods section except that parallel imaging is not available for the birdcage coil. C, Conductivity reconstruction based on the birdcage coil data. D, Conductivity reconstruction based on 20-channel head and neck coil data. The conductivity was reconstructed as described in the methods section using the simultaneously obtained B_1 map for the "full" complex electrical properties tomography (EPT) method. E, Histogram showing the distribution of the obtained conductivity values in the range between 0 S/m and 0.8 S/m for both coils. In this range, the birdcage and the head and neck coil yield a mean conductivity value of (0.37 $\pm$ 0.09) S/m and (0.36 $\pm$ 0.10) S/m, respectively.